Applied Catalysis A: General 527 (2016) 36–44

Contents lists available at ScienceDirect

Applied Catalysis A: General

journal homepage: www.elsevier.com/locate/apcata

Enhancement of high temperature metallic catalysts: Aluminum titanate in the nickel-zirconia system

D.R. Driscoll [a,*], M.D. McIntyre [b], M.M. Welander [b], S.W. Sofie [a], R.A. Walker [b]

[a] Department of Mechanical and Industrial Engineering, Montana State University, Bozeman, MT 59717, United States
[b] Chemistry & Biochemistry Department, Montana State University, Bozeman, MT 59717, United States

ARTICLE INFO

Article history:
Received 1 June 2016
Received in revised form 20 August 2016
Accepted 24 August 2016
Available online 24 August 2016

Keywords:
Infiltration
Catalyst stabilization
Thermal coarsening
Catalyst enhancement

ABSTRACT

Solution infiltration remains limited in its advantage for processing metallic catalysts given the propensity at high temperatures for nanometer scale materials to coarsen at rates far exceeding classic systems. Using SOFC anodes as a model system, this study examines how aluminum titanate as an additive to a porous Ni/YSZ cermet anode stabilizes a network of sub-micron nickel electrocatalysts formed from solution infiltration. Temperature dependent secondary phase formation is studied with XRD and Raman. Spatial evolution of the secondary phases that form is quantified using SEM/TEM/EDX to establish the species present during the thermal activation process. Finally, these results are used to fabricate SOFC membrane electrode assemblies, demonstrating the ease with which aluminum titanate can be added to nickel catalyst systems and the efficacy of the doping process. Current density and EIS measurements indicate that using aluminum titanate as an anode additive dramatically increases catalyst stability such that the time required for degradation to 90% of initial current output was increased by a factor of 115 for modified catalysts.

1. Introduction

Stability of catalyst microstructure, particularly for high-temperature metallic catalysts, is an important issue in a multitude of applications, particularly where nano-scale, high surface area materials are utilized. The attrition of precious metals from automotive catalytic converters has been sufficient to motivate studies that investigate the environmental impacts or harvesting of platinum group metals from roadside soils [1–4]. In another application, microstructure instability is a defining issue in implementing infiltration based anodes in Solid Oxide Fuel Cells (SOFC). The general consequences of metal catalyst coarsening are reflected by the need for addition of excess catalyst during device fabrication and in decreased device efficacy as fine catalyst microstructure coarsens. In this work, improvements to the microstructural stability of high-temperature metallic catalysts are explored using SOFC anodes as a model system in which catalyst percolation adds a primary constraint on system function. Specifically, this work uses the nickel metal/yttria-stabilized zirconia (YSZ) composition.

Traditionally, SOFC anodes are made of a ceramic/metal (cermet) composite material consisting of a nickel metal catalyst and yttria-stabilized zirconia (YSZ). Nickel provides an inexpensive catalyst when compared to less abundant materials in the platinum metals group. Ni retains high catalytic activity at the elevated operating temperatures of SOFCs, and over years of development has been established as the standard material for benchmarking performance [5–7]. Fabricating Ni-based cermet electrodes usually involves mixing nickel oxide, YSZ, and a pyrolizable thermal fugitive to achieve an equal volume mixture. This distribution of materials satisfies the percolation limit (3-D connectivity) allowing for simultaneous gas flow and electron flow through the anode, with ion transport extended farther into the anode than the planar anode-electrolyte interface. While this method is convenient for commercial production, it has several shortcomings. The high nickel concentration of over 33 vol% limits the mechanical strength of the YSZ and shifts the coefficient of thermal expansion for the anode to approximately 13.4 ppm/°C, much higher than that of the YSZ electrolyte (~10.8 ppm/°C). Mechanical stresses induced by thermal cycling can be detrimental to a cell/stack stability and cause catastrophic failures [8]. From a weight perspective, the density of nickel, 8.9 g/cc, is substantially higher than that of YSZ at 5.9 g/cc. The high solids loading of nickel therefore can also result in increased system mass which can be critically important in mobile applications. This consideration is compounded by a percentage of the nickel existing within the bulk of the cermet, not electroni-

* Corresponding author.
E-mail address: david.driscoll1@msu.montana.edu (D.R. Driscoll).

http://dx.doi.org/10.1016/j.apcata.2016.08.020
0926-860X/

cally connected to the anode structure and not contributing to the electrochemically active three phase boundary.

A different approach to anode fabrication is to introduce the nickel electrocatalyst by infiltration methods. Instead of being a simple mixture of sintered Ni and YSZ particles, an infiltrated electrode starts with a YSZ scaffold rendered porous by one of several available methods. These methods include pyrolyzable thermal fugitives, freeze tape casting which leaves porosity in a green state, or a chemical leaching method [9–11]. The sintered, porous YSZ is then infiltrated with a solution-based nickel precursor such as nickel nitrate. Similar methods have also been established for infiltration of common lanthanum-based perovskite cathodes [8,12–15]. Use of infiltration for both the fuel and air electrodes lends itself to a symmetrical cell architecture where porous scaffolds can be applied to both sides of the electrolyte resulting in a design that is scalable both in size and in quantity [16,17].

Depositing catalysts on a pre-existing scaffold via infiltration significantly reduces the amount of catalyst material required. Given an appropriate scaffold geometry, as little as 15 vol% of expensive [18], high mass density catalysts could be used to produce fuel cell electrodes with excellent thermal expansion coefficient matching. Cells produced in this manner have already shown excellent redox stability while retaining high catalytic activity [12,19–21]. Because the scaffold and catalyst are processed in discreetly different steps means that catalysts previously precluded due to high temperature reactivity with electrolyte materials can be considered as viable options for development. For example, lanthanum strontium manganite (LSM) reacts with YSZ at temperatures above 1200° C to form $La_2Zr_2O_7$, an ionic insulator [22]. This undesired outcome constrains how SOFC membrane electrode assemblies are fabricated, given that LSM is often used as an SOFC cathode and YSZ is one of the most commonly used SOFC electrolytes. Moreover, material combinations for low temperature-SOFCs that were previously considered impractical due to reactivity between phases at processing temperatures also become feasible with infiltration [23]. Infiltrated cells localize catalysts where they are most needed for activity and catalyst particles formed from infiltration tend to be much smaller than those used in mechanically mixed electrodes. Furthermore, smaller catalysts have power densities that far surpass the performance of traditional SOFC cermet electrodes [17,19,24–26].

In high temperature applications, the advantages of electrode fabrication by infiltration have not been fully realized. This is due largely to the fact that very fine nickel metal introduced by infiltration at particle diameters < 100 nanometers migrates and coarsens substantially, degrading cell performance at rates much greater than traditional anodes. At SOFC operational temperatures (700 °C to 1000 °C) small nickel catalysts have been shown to coarsen and agglomerate into larger particles that break up the original nickel network. This behavior leads to two important problems; first, the larger particles are less catalytically active than the smaller, original network of particles due to the substantial decrease in surface area (reduced triple phase boundary length). Second, the coarsening of nickel causes voids and separation in the nickel network, breaking down the electron path for current collection and hindering overall performance of the anode [25–29].

Recent reports have shown that adding a minor amount of secondary phase additive, such as aluminum titanate (Al_2TiO_5 or ALT), improves the performance of Ni-infiltrated SOFC cermet anodes [30]. The proposed mechanism of improved anode stability cited chemical interactions between the catalyst and substrate in which portions of the nickel network that had previously necked down to a discontinuous path were instead stabilized at 800 °C [30,31]. This work suggested that high temperature reaction of the Ni-YSZ-ALT system led to the formation of additional oxide phases, $NiAl_2O_4$ and $ZrTiO_4$, within the anode; however, the spatial distribution and phase evolution of the secondary phases remained uncharacterized. Furthermore, $NiAl_2O_4$ and $ZrTiO_4$ are not expected to exhibit electro-catalytic behavior to facilitate electrochemical function despite the loss of primary phases [32,33]. If these secondary phases stabilize small particles at high temperatures, these materials can be strategically added to stabilize nanoscale supported catalysts. This approach may be applied to several industries where migration of a catalyst or metal phases on a ceramic oxide surface has been shown to lead to failures such as automotive catalytic converters [34], methane reforming systems [35], and multilayer capacitors [36], as well as SOFCs [7,28,29,37].

In order to explore the electro-catalyst enhancement of ALT additions in traditional SOFC anodes, experiments described below identify the reaction pathways that form multiple secondary phases in the nickel/zirconia system. Phase formation as a function of temperature during standard anode processing temperature regimes was evaluated using complementary XRD and Raman spectroscopy data. The spatial distribution and morphology of the secondary phases with regard to the nickel/zirconia interfacial region were assessed with FIB/TEM analysis and the mitigation of nickel coarsening/spallation identified by SEM analysis of post-tested nickel electro-catalysts. Voltammetry and Electrochemical Impedance Spectroscopy (EIS) measurements were performed to examine how the dopant influences degradation in the doped and undoped systems. The merits of using SOFC anodes as a model catalyst/support system to study these enhancement mechanism(s) are bolstered by the attributes of a truly high temperature system (700–1000 °C) combined with the added rigor of requiring catalyst percolation for electronic conductivity.

2. Experimental

2.1. X-ray diffraction

Previous studies had performed XRD scans at coarse temperature intervals to find evidence of secondary phase formation and to establish pertinent reaction temperatures [30]. In this study, a scan of temperature intervals ranging from 1100 °C to 1400 °C was completed to identify specific formations, intermediate phases, and a more precise temperature window that provide tailorability of the system. Powder mixtures of NiO (Alfa Aesar, 12359), YSZ (Tosoh, 8YS-YSZ), and Al_2TiO_5 (Alfa Aesar, 14484) were prepared at 12.1% ALT, 29.4% YSZ, and 58.5% NiO on a molar basis. This ratio corresponded to equal bulk volumes of the three constituents. The mixture was pressed into pellets in a 1.9 cm diameter die at 172 MPa and heated to temperatures between 1100 and 1400 °C at 5 °C/min up and 10 °C/min down with a 1 h dwell. Post sintering, pellets were ground back to a powder in a Diamonite mortar and pestle and scans were taken from 20° to 70° 2θ with an XRD (Scintag Inc. XGEN-4000). Powder spectra were then compared to relevant powder diffraction files and compared to other temperatures.

2.2. Raman spectroscopy

Complimentary Raman spectroscopic measurements were performed on the same samples following XRD measurements. A Renishaw InVia spectrometer equipped with an edge filter (~150 cm^{-1} cutoff) and 50 x microscope objective collected the Stokes-scattered light from a 488 nm Ar-ion laser (18 mW). Room temperature spectra were recorded with a 10 s exposure and 1 accumulation per spectrum.

2.3. Microscopy and elemental analysis

Samples were prepared specifically for examination by TEM and contained significantly higher ALT percentages than practical for

use in electrochemical cells to ensure the location of pertinent secondary phases for imaging and chemical characterization. Three FE-SEMs with Focused Ion Beam Milling attachments were used at the Environmental and Molecular Sciences Laboratory (FEI Helios, and two FEI Quanta) for detailed elemental mapping and to prepare samples for HR-TEM (Titan 80–300). Samples of 50 wt%YSZ and 50 wt%ALT were freeze tape cast in aqueous solution as described elsewhere [9,38]. Freeze tape casting was utilized to produce an ordered, columnar pore surface for ease of identification and FIB cross-sectioning of catalyst/support interfaces for TEM analysis. Using a 2.5 cm diameter punch, disks were cut from the tape and sintered up to 1400 °C with 1 h dwell at a rate of 5 °C/min up and 10 °C/min back down to room temperature. The nickel electrocatalyst was applied in a fashion consistent through this study. Nickel nitrate ($Ni(NO_3)_2$*$6H_2O$, Advanced Materials, 28C-NT-01), was applied to the surface of the disks until saturated, then placed under a vacuum for 60 s to prevent bubble entrainment. The samples were placed in a 500 °C furnace to decompose the nickel nitrate and form nickel oxide. Infiltration was then repeated until loading reached the desired threshold. The sample with ALT in the bulk was placed in the furnace and heated to 1400 °C to activate the anchors with a 1 h dwell and the standard heating and cooling rate of 5 °C/min and 10 °C/min, respectively. Samples were finally exposed to a reducing atmosphere of 5%H_2/95%N_2 at 800 °C for 48 h. This allowed the nickel oxide to reduce and mild thermal coarsening to occur with the intention of easing the location of the secondary phases for the microscope studies. Disks were placed in the SEM with FIB and, through the focused ion beam attachment, samples of approximately 10 μm in width were removed for TEM/EDS analysis. EDS and TEM analysis were performed on the same FIB cross sections so as to render the penetration depth of EDS a non-issue in correlating TEM images with EDS determined composition.

2.4. Electrochemical cells

Cell fabrication and electrochemical testing was carried-out in a manner consistent with the formation of ALT anchors as detailed previous work [31]. Significantly, a major focus of this effort was to compare multiple ALT doped and traditional cells at a fixed and known catalyst loading. The electrolyte supported cells were based on commercially available electrolytes (Fuel Cell Materials, 211103) composed of 8 mol% yttria YSZ and were approximately 300 μm in thickness with a diameter of 32 mm. Electrode scaffolds were applied through aerosol spraying of an aqueous mixture of YSZ and cornstarch in a 40:14 mass ratio with appropriate binder (Ethyl Cellulose, Sigma-Aldrich 200646), plasticizer (PEG 200, Sigma Aldrich, P3015), and dispersant (R.T. Vanderbilt Co., Darvan C-N). Once sprayed and dried at 70 °C, the scaffolds were sintered to 1200 °C for 1 h with heating and cooling rates of 5 °C/min. In this way, prepared electrode scaffolds were 50 μm thick with approximately 40% porosity and 28 mm diameter.

In each cell, the anode was infiltrated prior to and separately from the cathode. In undoped cells, those without Al and Ti additives, a solution of 6 M nickel nitrate ($Ni(NO_3)_2$*$6H_2O$, Advanced Materials, 28C-NT-01), where the hydrated state of the nitrate was considered, was added to the scaffold via pipette. Solution was added until the scaffold was fully saturated with the infiltrant. The nitrate was then decomposed in a box furnace at 400 °C ultimately yielding NiO [39]. This process was then repeated until a catalyst loading of 20% of the total (YSZ + porosity) scaffold volume had been achieved utilizing an analytical balance (Sartorius, CPA225D) to track infiltration loading. Using three un-infiltrated cells with sintered porous scaffolds, a combination of FE-SEM study and mass measurement revealed the scaffold bulk density prior to infiltration to be 2.3 g/cm^3. For all cells loaded with catalyst, a density of 6.67 g/cm^3 for NiO and the measured scaffold density were used with repeated mass measurements to obtain 20 vol% catalyst loading. Doped cells were infiltrated with a catalyst solution of nickel nitrate ($Ni(NO_3)_2$*$6H_2O$, Advanced Materials, 28C-NT-01), aluminum nitrate ($Al(NO_3)_3$*$9H_2O$, Fluka, 06275), and titanium lactate ($C_6H_{18}N_2O_8Ti$, Sigma-Aldrich, 388165) in the correct stoichiometry to produce NiO with Al_2TiO_5 at 2 mol%. Ultimately, this yielded 2mol% ALT in NiO infiltrated to 20vol% of the electrode scaffold. Infiltrated anodes were then sintered to 1400 °C, which had been previously shown to impart efficacy of the ALT doping strategy [30].

Cathodes were prepared identically across all tested cells and then infiltrated in a similar fashion using a combination of nitrates in the correct stoichiometry to form $(La_{0.6}Sr_{0.4})_{0.95}FeO_{3-x}$. A density of 6.24 g/cm^3 was assumed for LSF in achieving a loading of 20 vol%. Complete cells with the cathode were sintered to 900 °C for 1 h to allow formation of the ABO_3 perovskite phase from the precursors prior to cell testing.

Cells were tested in a clamshell furnace which held a seal-less Inconel platen-type test fixture, dedicated to clean runs, described elsewhere [40]. Gas flow control was accomplished using a MKS 647C flow control system. Silver mesh was used at the cathode with nickel foam at the anode and joints completed with a paste made from AgO (Alfa Aesar, 43268) dispersed in xylene to create electrical continuity. Copper wire affixed to the Inconel platens connected in series with the cell and Agilent N3301A electronic load and Agilent 6651A power supply. Cathodes were fed air from a zero air generator, and anodes were fed a humidified hydrogen nitrogen mix. Gases were flowed at a ratio of $3N_2$: $4H_2$ to the anode. All cells were run at 850 °C and 0.7 V unless otherwise noted [41–43].

2.5. Electrochemical impedance spectroscopy

In order to characterize how the electrochemical processes differ between the doped and undoped cells, EIS experiments were conducted on the each of the cell types. A silver mesh current collector was secured to the cathode with platinum paste while a gold mesh current collector was attached to the anode with gold paste to ensure that the anodic reactions were completely due to the electrode material. The cell was secured to an alumina tube with alumina paste (Ceramabond 552-VFG, Aremco), which created a seal between the cathode and anode atmospheres, and heated to 800 °C at a rate of < 1 °C in a custom designed assembly described elsewhere [44,45]. The LSF cathode was exposed to air (85 ml/min) and the anode was exposed to 50:50H_2: Ar (each at 100 ml/min) gas mixture. EIS was collected with a Princeton Applied Research VersaStat MC over a frequency range of 100,000–0.1 Hz with rms amplitude of 10 mV. Prior to and post polarization, EIS was recorded at open circuit voltage (OCV). Degradation under polarization was evaluated by collecting EIS throughout the course of each experiment where the cell was held at 0.7 V for 16.5 h.

3. Results & discussion

3.1. Al_2TiO_5-NiO-YSZ reaction study

XRD and Raman characterization in this work establish reaction products, that include secondary phases, as a function of temperature. The presence of these materials, post-processing, frame the mechanisms proposed for catalyst anchoring. Characterization of samples at processing temperature intervals of 50° from 1000 °C to 1400 °C yielded unanticipated findings showing the formation of desirable secondary phases and potentially deleterious phases. Powder mixtures used for this study contained ALT concentrations elevated higher than would be used for anchoring in electrochem-

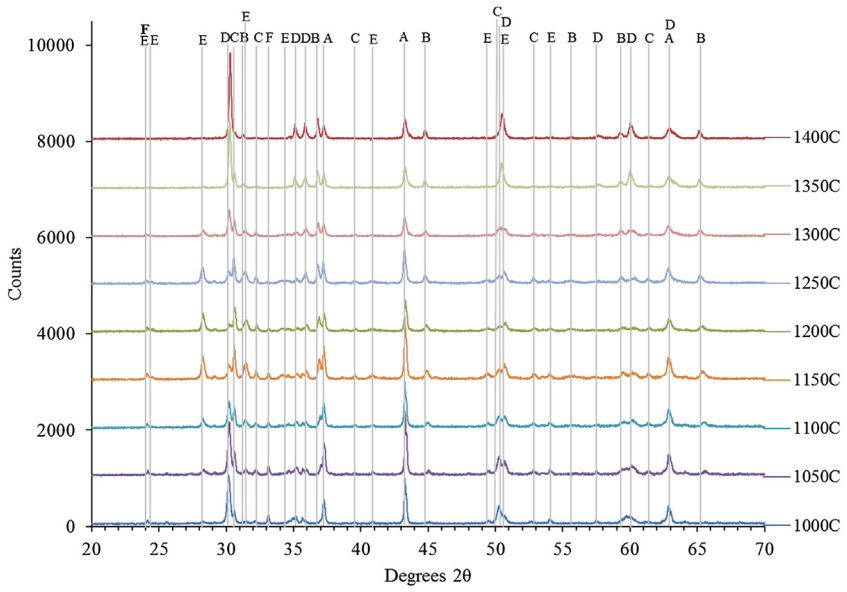

Fig. 1. Complete XRD patterns for NiO/YSZ/ALT mixture from 20 to 70° 2θ and reaction temperatures ranging from 1100 °C–1400 °C. Phases are identified as follows. A: NiO, B: $NiAl_2O_4$, C: $Zr_5Ti_7O_{24}$, D: YSZ, E: *m*-ZrO_2, F: $NiTiO_3$.

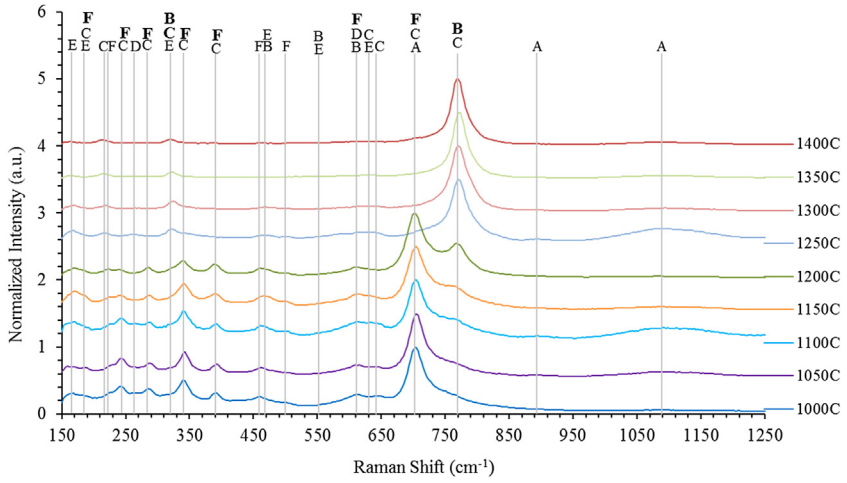

Fig. 2. Normalized Raman spectra from ALT-Ni-YSZ samples showing compositional changes as a function of sintered temperature ranging from 1000 to 1400 °C. Spectra have been offset for clarity. Phases are identified as follows. A: NiO, B: $NiAl_2O_4$, C: $Zr_5Ti_7O_{24}$, D: YSZ, E: *m*-ZrO_2, F: $NiTiO_3$.

ical cells in order for all relevant phases to be observable given the 3–5% detection limits of XRD methods. Raman spectroscopy provides complementary chemical analysis to validate XRD results.

The complete XRD patterns and Raman spectra are presented in Figs. 1 and 2, respectively. Due to the complex nature of relating phase evolution at 9 temperatures over 20–70° 2θ, windows of small 2θ range are presented containing representative peaks used for product identification. These results are summarized in Table 1 that reports phase formation as a function of temperature. Fig. 1 highlights cubic YSZ (~30° 2θ) being destabilized in favor of monoclinic ZrO_2 (~28° 2θ) at intermediate temperatures, NiO (~43° 2θ) persisting at all temperatures, secondary phase $NiAl_2O_4$ (~37° 2θ) increasing in concentration with reaction temperature, and secondary phase $Zr_5Ti_7O_{24}$ (30.7° 2θ) reacting for maximum concentration at around 1200 °C and then decreasing in prevalence until it is barely detectable at 1400 °C. Fig. 2 shows complementary Raman spectra that illustrate how sintering temperature effect the formation of the secondary phases in a similar manner to the XRD data. The most intense vibrational modes associated with YSZ at ~620 (615 cm^{-1} for the cubic phase and 630 cm^{-1} for the tetragonal phase) and NiO at 1090 cm^{-1} are present at all temperatures. The feature at 615 cm^{-1} corresponding monoclinic ZrO_2 appears in spectra collected from samples sintered at 1000–1300 °C. The strongest signals from the $Zr_5Ti_7O_{24}$ secondary phase at 214 cm^{-1} and 322 cm^{-1} begin to grow in at 1100 °C and are visible at the higher temperatures. Interestingly, the $NiTiO_3$ and $NiAl_2O_4$ secondary phases exhibit an inverse relationship with the amount of $NiTiO_3$ decreasing as temperature increases and disappearing ≥ 1250 °C while $NiAl_2O_4$ forms more readily at the higher temperatures >1050 °C.

Fig. 3 contains all diffraction patterns from 1000 °C to 1400 °C over the 23–29° 2θ range with the representative peaks of m-ZrO_2 and $NiTiO_3$ labeled. ALT was not observed by Raman or XRD at any of the tested temperatures indicating complete, or nearly complete, decomposition. At sintering temperatures between 1000 °C–1300 °C, monoclinic zirconia is observed despite the 8 mol% yttria in the beginning YSZ. This destabilization of YSZ is discussed with the additional context of Fig. 4 at the end of this section. Finally, in the temperature range of 1000 °C to approximately 1250 °C, the unanticipated presence of a $NiTiO_3$ is observed. Forma-

Table 1
Summary of temperature dependence in phases observed by XRD and Raman.

°C	c-ZrO_2	m-ZrO_2	NiO	$NiAl_2O_4$	$Zr_5Ti_7O_{24}$	$NiTiO_3$
1400	Strong	Not Detected	Strong	Strong	Detected	Not Detected
1350				Increasing with Temperature		
1300		Detected			Strong	
1250	Detected	Strong				Detected
1200						
1150						
1100	Strong	Detected				
1050						
1000				Not Detected	Detected	

tion of these phases is corroborated by Raman spectra with strong vibrational bands at 702 cm^{-1} for $NiTiO_3$ and 169 cm^{-1} for m-ZrO_2 [46].

Fig. 4 shows XRD data in an expanded range from 29.7 to 30.9° 2θ. The two features that appear identify cubic and tetragonal yttria-stabilized zirconia at approximately 30.2° 2θ and $Zr_5Ti_7O_{24-x}$ at approximately 30.7° 2θ. The $Zr_5Ti_7O_{24-x}$, secondary phase is detectable at all temperatures with maximum concentrations observed at 1150 °C–1200 °C, the same temperature window where m-ZrO_2 concentrations were also maximized. $Zr_5Ti_7O_{24-x}$ is confirmed in the Raman spectra with vibrational bands at 214 and 322 cm^{-1} [47]. The YSZ identifying peak in the XRD undergoes a shift to larger angles in samples sintered at higher temperatures indicative of a shrinking lattice parameter. This result is explained by the smaller Ti^{4+} substituting for Zr^{4+} in the YSZ lattice as the $Zr_5Ti_7O_{24}$ decomposes at high temperatures leaving additional Ti to dissolve into the YSZ lattice [48].

The presence of $Zr_5Ti_7O_{24-x}$ may be beneficial from an electrochemistry perspective. Given the necessity of Y_2O_3 for the formation this phase, oxygen vacancies would be required by the reaction proposed here [47,49,50]:

$$Y_2O_3 \rightarrow 2Y'_{Zr} + V_{\dot{O}} + 3O_o^x$$

The discovery of $Zr_5Ti_7O_{24}$ with oxygen vacancies suggests the potential of an electrochemically active secondary phase associated with the generation of oxygen ion conductivity and potentially associated electronic conductivity as a result of charge compensation.

The remaining interactions of nickel with ALT to form anchoring phases are presented in Fig. 5. The peak at 63° 2θ corresponds to NiO, which is observed at all temperatures between 1000 °C and 1400 °C, as expected. The peak at approximately 65.5° 2θ represents $NiAl_2O_4$, another secondary phase that can play an important role in catalyst anchoring. The relative amount of $NiAl_2O_4$ steadily increases with temperature.

The absence of ALT, TiO_2, and Al_2O_3 at any temperature combined with the formation of $NiAl_2O_4$ by 1050 °C and $Zr_5Ti_7O_{24}$ at 1000 °C suggests that temperatures as low as 1050 °C are sufficient to form secondary phases from the ALT and its decomposition products. The formation of *m*-ZrO_2 beginning at 1000 °C is concerning in an anode environment due to the lack of this phase's ionic conductivity. The appearance of *m*-ZrO_2 is not surprising, how-

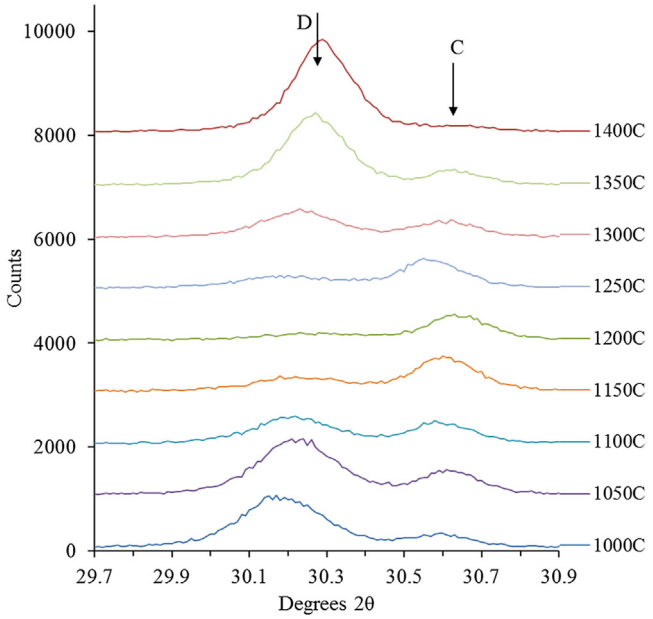

Fig. 4. Cu-kα X-ray diffraction of the Al_2O_3/TiO_2/NiO/YSZ powder mixture in the 29.7–30.9° 2θ range. All samples were heated at 5 °C/min up and 10 °C/min down with a 1 h dwell. Phases are identified as follows C: $Zr_5Ti_7O_{24}$, D: YSZ.

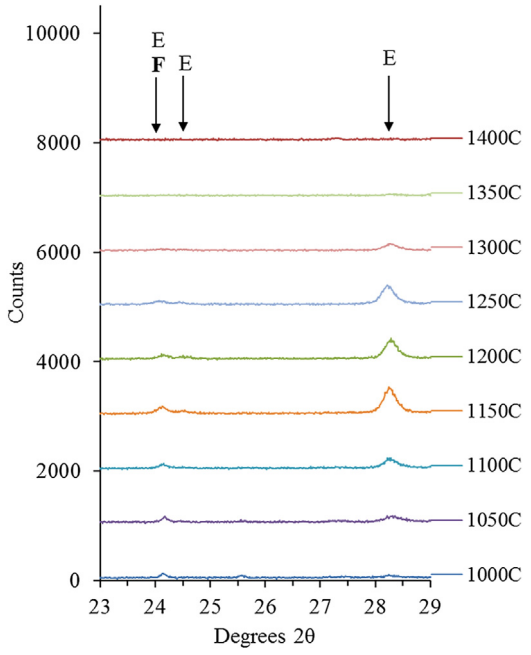

Fig. 3. Cu-kα X-ray diffraction of the Al_2TiO_5/NiO/YSZ powder mixture in the 23–29° 2θ range. All samples were heated at 5 °C/min up and 10 °C/min down with a 1 h dwell. Phases are identified as follows. E: *m*-ZrO_2, F: $NiTiO_3$.

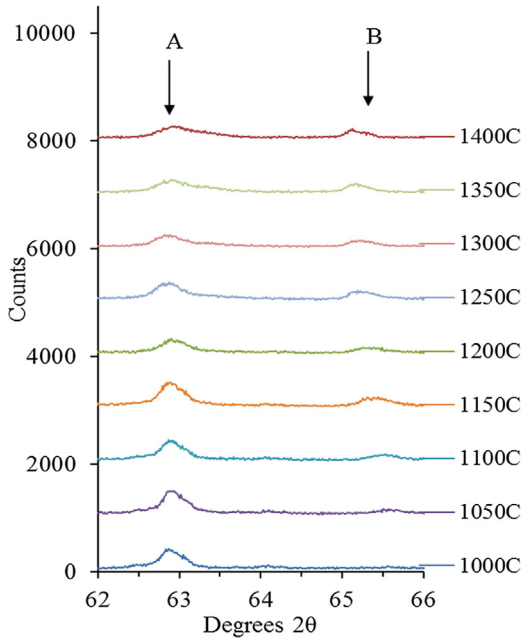

Fig. 5. Cu-kα X-ray diffraction of the Al_2O_3/TiO_2/NiO/YSZ powder mixture in the 62–66° 2θ range. All samples were heated at 5 °C/min up and 10 °C/min down with a 1 h dwell. Phases are identified as follows. A: NiO, B: $NiAl_2O_4$.

ever, as $Zr_5Ti_7O_{24}$ formation is reported to require the presence of small amounts of yttria [47,51,52]. Consequently, recruiting Y for the zirconium titanium oxide will leave *c*-YSZ yttria deficient and destabilize the ionically conducting cubic phase. The concentration of the monoclinic phase begins to fall dramatically at temperatures above 1300 °C. Finally, the formation of $NiTiO_3$ was not anticipated and was observed in small quantities over a limited temperature range with both XRD and Raman methods. To optimize this system for maximum catalytic efficiency and durability, formation of $NiTiO_3$ presents an attractive opportunity where it has been reported to be an active catalyst [53,54]. Future studies to form $NiTiO_3$ directly through infiltration may provide an alternate catalyst enhancement with a Ti-only doping scheme.

While XRD and Raman analyses of the NiO-YSZ-ALT system do not directly explain the ALT enhancement of catalyst stability, these results certainly illustrate the complexity of the system while providing a useful basis for determining ideal processing temperatures. Temperatures near 1300 °C ideally balance the high temperature requirement to form secondary phases thought to anchor catalysts and to avoid incorporating the insulating monoclinic ZrO_2 phase into the anode, with the low temperature advantage of maintaining significant concentrations of $Zr_5Ti_7O_{24-x}$ and $NiTiO_3$.

3.2. Microscopy and elemental analysis

XRD and Raman data in Figs. 1–5 show that a variety of phases form when a YSZ scaffold is infiltrated with nickel and ALT and that the relative abundance of these materials is strongly dependent on processing temperature. An important objective of this work is to establish the spatial distribution of secondary anchoring phases relative to nickel metal on YSZ to elucidate mechanisms that foster catalyst enhancement. The FIB cross-section in Fig. 6 provides direct evidence that ALT derived phases form in close proximity to the nickel catalyst by establishing the presence of Ni/Al and Zr/Ti mixtures at Ni/YSZ interfaces. EDS was utilized on FIB-prepared samples to identify the chemical composition of two grains of YSZ with a nickel particle as labeled and three additional grains. The original hypothesis for ALT catalyst enhancement, suggested a continuous composition gradient that progresses from YSZ to $ZrTiO_4$ to ALT to $NiAl_2O_4$ to nickel [30]. While XRD has already suggested that ALT does not exist in the thermally treated system, the discrete grains in Fig. 6 dispel the hypothesis of a composition gradient as had been suggested previously.

The right-hand panel of Fig. 6 contains EDS spectra corresponding to the labeled grains in the TEM image. Area 1, which sits adjacent to two YSZ grains, contains primarily the constituents of YSZ plus titanium. The spectrum also contains small amounts of nickel and copper. The copper, a known artifact of the TEM grid, can be dismissed. Most importantly, the co-presence of YSZ and titanium combined with results from XRD and Raman studies leads to the conclusion that a discrete grain containing largely Zr/Ti exists immediately adjacent to grains of YSZ where the solubility limit of Ti in YSZ is reported as about 10–15 mol% [55]. The role of the nickel in Area 1 is less clear. $NiTiO_3$ would be a clear candidate for existence within the grain at lower sintering temperatures, but nickel ions in solution with the ZrO_2 are also possible. As indicated by EDS, Area 2 is of very similar composition to Area 1. While the role of nickel in the grains is uncertain, these grains do provide direct evidence for the Zr/Ti secondary phase occurring at the boundaries of YSZ grains and nickel particles.

Area 3, immediately adjacent to the observed nickel, is composed of nickel and aluminum. Again corroborating with XRD and Raman results, this area is identified as $NiAl_2O_4$. Given that this sample was prepared from Al_2TiO_5, combined with the progression in Fig. 6 from YSZ to Zr/Ti to $NiAl_2O_4$ to Ni, suggests clear spatial progression of the secondary phases that serve to enhance fuel cell based electro-catalysts.

3.3. Electrochemical cells

While TEM observation identifies secondary phase formation at the interface between the catalyst and ceramic support in discrete grains, the influence of these phases is not fully understood. Electrolyte supported SOFCs with and without doped anode catalysts were studied by voltammetry and EIS to identify the electrochemical contributions of the secondary phases.

3.4. Ni metal coarsening

Current density curves were collected for cells with and without the ALT dopant. Fig. 7 shows SEM images of YSZ substrates infiltrated with Ni and with a Ni/ALT mixture. These structures, after being sintered at 1400° C in the manner described above, were then subjected to a reducing atmosphere at 800° C for 50 h. In comparing the Ni microstructure, evidence of nickel coarsening at 800 °C is readily apparent in the cell without ALT. ALT doping appears to restrict the Ni coarsening with average grain sizes after 50 h approximately half of that observed in the pure Ni. Moreover, heavy spallation of the Ni from the YSZ substrate is readily apparent in the pure specimen while essentially non-existent in the ALT doped sample. The clear difference in propensity for spallation suggests particle anchoring as a mechanism of performance enhancement in ALT doped anodes. This qualitative analysis corroborates the improvement of degradation rate associated with ALT use that is described below and provides context for discussion of that improvement.

3.5. Electrochemical cell degradation

The comparative performance of anodes infiltrated with ALT was determined by testing the efficiency and stability of four cells under a constant voltage at 0.7 V. Cells were fabricated with identical anode and cathode preparation, with the only difference being the addition of ALT to the anode of two cells. Stability data in Fig. 8

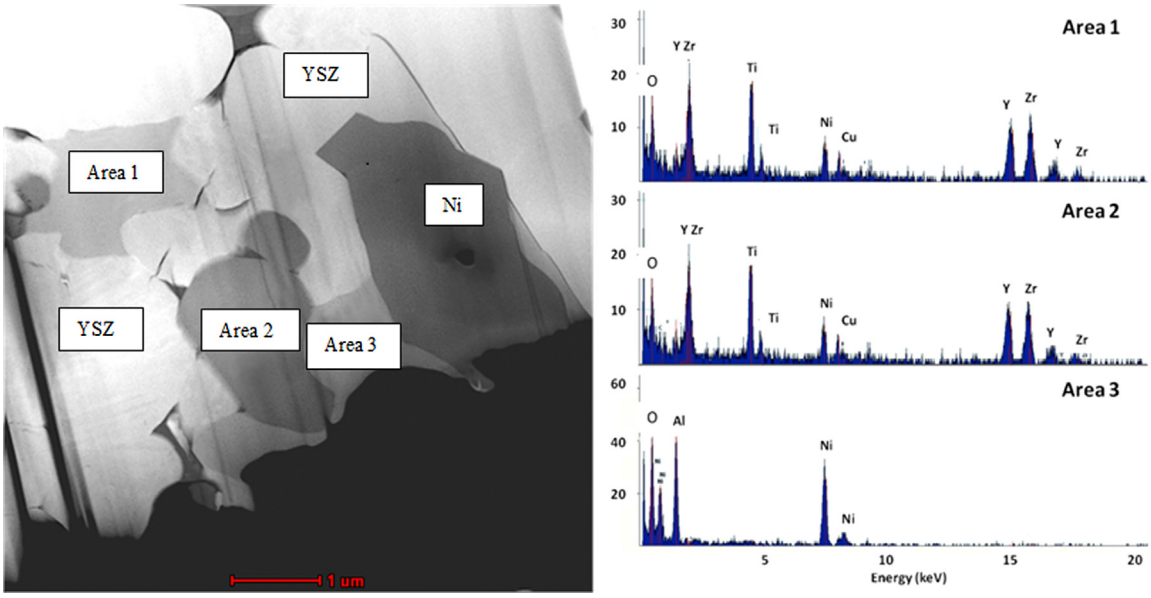

Fig. 6. TEM image and corresponding EDS analysis of FIB cross-section from YSZ/ALT tape cast infiltrated with nickel nitrate and then reduced.

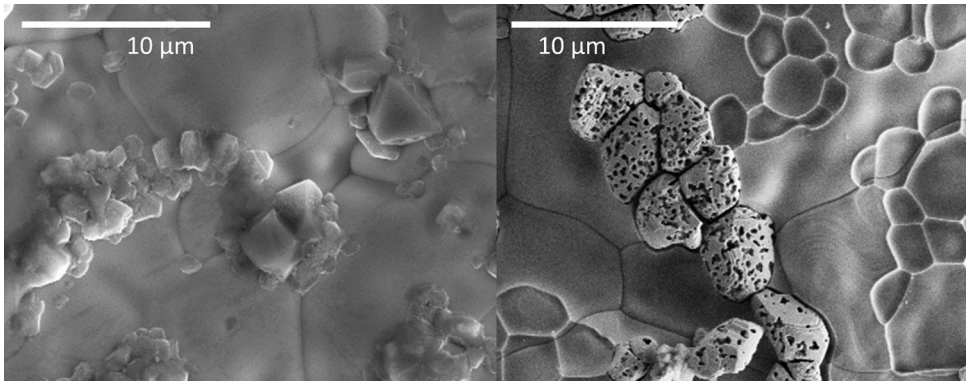

Fig. 7. FESEM images of nickel on YSZ electrolytes. Left: ALT-doped nickel, and Right: Pure nickel. Substrates were coarsened for 50 h in a reducing atmosphere at 800 °C.

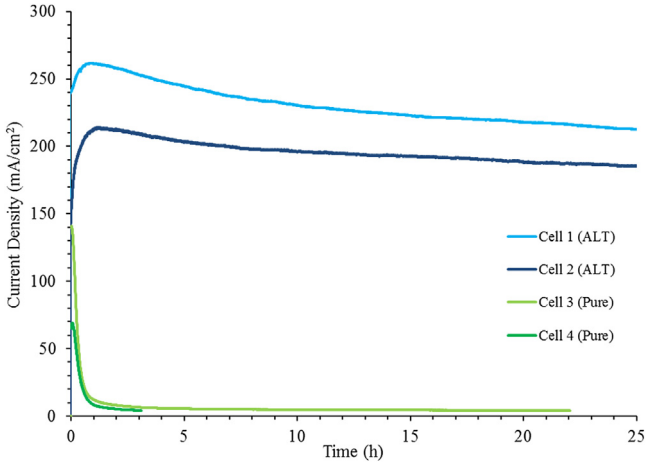

Fig. 8. Specific current output over the first 25 h of operation for 4 infiltrated cells. All cells were run at a constant 0.7 V and 850 °C with humidified H_2/N_2 fed to the anode. ALT cells had 2 mol% Al_2TiO_5 precursors in the Ni infiltrant. Pure cells had Ni only infiltrated into the anode.

shows that the cells had an initial current output of ~215 mA/cm^2, a value that is reasonable given an electrolyte thickness of 300 µm. Based on the initial catalyst particle size of 50–100 nm and low Ni loading, nickel coarsening was anticipated for all four identical cells [56].

Cells prepared without the ALT infiltration dopant showed extensive degradation, demonstrating a loss in current density by more than 90% in less than 5 h. The stabilizing effect of the secondary phases formed by reactions of ALT with Ni and YSZ is shown, however, to be quite profound. The two non-treated cells lost 93% and 96% of their maximum observed performance within two hours of operation at the tested anode loading levels. At the same time, Cells 1 & 2 with the ALT additions degraded by only 1.6% and 0.7%. The substantial difference at a short time scale is especially important given a relatively low catalyst loading, designed to exaggerate degradation due to a loss of nickel percolation associated with coarsening. Given the material changes within the ALT modified anode and the *ex situ* distribution of phases observed after operation, the severity of current degradation and microstructural changes without ALT addition suggest that the secondary phases create a more robust catalyst network by means of enhanced interaction between the catalyst and the YSZ support phase, limiting thermally induced degradation.

3.6. Electrochemical impedance spectroscopy

EIS measurements were performed on ALT modified and unmodified cells having slightly higher catalyst loading to further

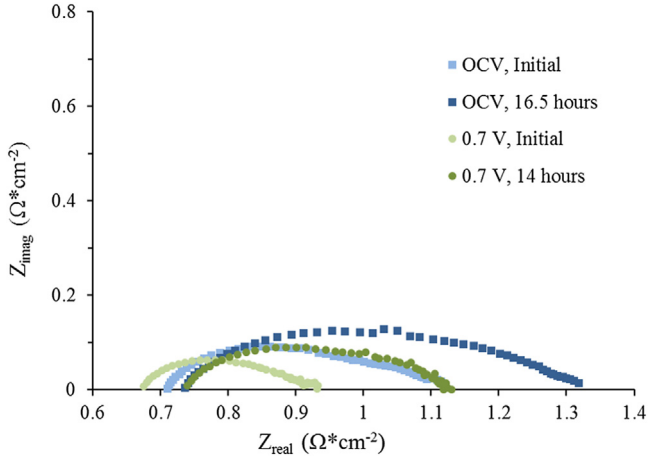

Fig. 9. EIS data from a cell with a pure Ni-YSZ anode at 800 °C and at OCV or held at 0.7 V. Both R_B and R_P increased during and following 16.5 h of polarization in which the current density decreased by ~22%.

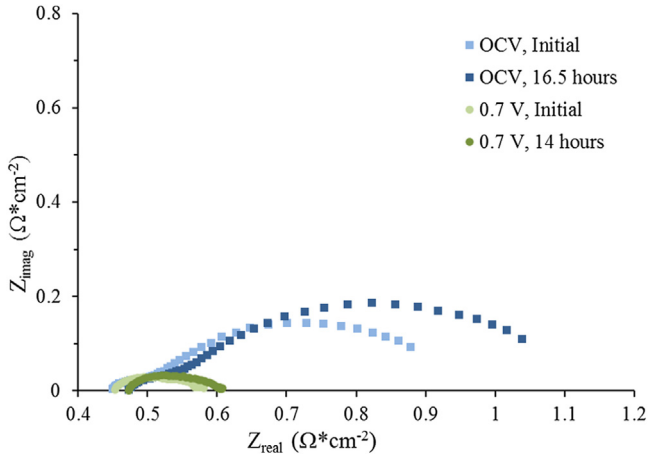

Fig. 10. EIS data from a cell doped with a 2 mol% ALT at 800 °C at OCV or held at 0.7 V. Both R_B and R_P increased during and following 16.5 h of polarization in which the power density decreased by ~9%. The large impedance measured at OCV suggests that the ALT doped should not perform better than the pure cell during polarization; however, the EIS under 0.7 V has lower impedances than the pure cell that corresponds to the observed improved specific power. The lower polarization resistances result from the secondary phases in the ALT doped cell with mixed ion-electron conducting properties.

elucidate the electrochemical effects of ALT additions to the anodes. Cells for EIS analysis were prepared in an identical manner to those for the current density measurements. Impedance spectra for the pure and ALT doped cells are shown Figs. 9 and 10 respectively.

Under initial OCV conditions, the pure cell had a polarization resistance (R_p) of 0.428 Ω*cm^{-2} compared with 0.489 Ω*cm^{-2} for the ALT doped cell, a result that is consistent with expectations given an anode doped with non-conductive Al/Ti oxides [32,33]. However under polarization (0.7 V), R_p decreased to 0.253 Ω*cm^{-2} for the pure cell and to 0.126 Ω*cm^{-2} for the ALT doped cell. The marked reduction in R_p upon polarization for the ALT cell over that of the pure cell can be attributed to mixed ion-electron conductive properties of Zr/Ti oxides that only become functionally active under polarization [49,50,57].

Further illustrating the influence of ALT in the anode system is the change in R_p as the cells were run. Spectra were taken under polarization at 10 min and 14 h. The pure cell experienced in increase in R_p from 0.253 Ω*cm^{-2} to 0.379 Ω*cm^{-2}. The ALT cell transitioned from 0.126 Ω*cm^{-2} to 0.134 Ω*cm^{-2} implying that the structure and electrochemical properties of the ALT modified anode changed very little while the unmodified anode underwent significant change over the course of 14 h. Changes in R_p over the 14 h time scale of interest are attributed to the anode microstructure given 1) the ~100 nm initial particle size, 2) still low catalyst loading, and 3) changes in the EIS spectra occurring at the low frequency intercept. The stabilization in R_p for ALT doped cells suggests that ALT has a profound affect in preserving the electronic percolation of the anode microstructure. R_p at OCV conditions increased from 0.428 Ω*cm^{-2} to 0.580 Ω*cm^{-2} (35.7%) for the pure cell, and from 0.489 Ω*cm^{-2} to 0.648 Ω*cm^{-2} (32.5%) for the ALT cell.

In a more predictable manner, bulk resistance (R_B) was essentially unchanged in the transition from the open-circuit to polarized state. However, initial R_B was substantially smaller for the ALT doped cell (0.448 Ω*cm^{-2}) than the pure cell (0.682 Ω*cm^{-2}). This result could indicate a greater density in the anode scaffold which is corroborated by the larger low-frequency arc in the ALT sample than the pure, and further consistent with observations of ALT functioning as a sintering aid [58]. Additionally, decreased R_B in the ALT doped anode may be founded in the formation of the observed $Zr_5Ti_7O_{24}$ phase which has been reported to possess an extent of electronic conductivity [55]. Over the course of the 16.5 h experiment, R_B for the ALT doped cell increased by 5.5% and pure cell by 8.1%.

4. Conclusions

ALT doping of the Ni/YSZ system has yielded dramatically increased catalyst stability in low catalyst loading SOFC anodes. Characterization of this system has provided insight into the formation of phases which are proposed to contribute to improved catalyst thermal resilience as well as processing conditions which offer maximum efficacy. XRD and Raman have suggested that from the perspective of Zr/Ti oxide formation, and stability of the cubic phase in YSZ, temperatures at or above 1300 °C should be beneficial. TEM imaging has provided direct observation of anchoring phases in appropriate spatial relation to the Ni and YSZ phases. Finally, ALT modified electrochemical cells have demonstrated profoundly decreased degradation rates relative to non-doped cells such that the time required for degradation to 90% of initial current output was increased by a factor of 115. EIS has simultaneously indicated that improved degradation rates can be indeed be attributed to the anode and that additions of Al/Ti dopants influence changes apparent only under polarization. This observation calls for detailed study of the Ni/anchoring phase interface. The use of ALT at low concentrations, while yielding small impacts to the processing of SOFCs, offers substantial improvement to the microstructural stability of nanometer scale infiltrated catalysts.

Acknowlegements

This work was supported by the NSF under grant #DMR-1411210. The authors also acknowledge the analytical characterization at the Environmental Molecular Sciences Laboratory (EMSL) at PNNL through a rapid access grant #43791. FEM and XRD data were collected at the MSU Image and Chemical Analysis Laboratory. Additionally, the authors gratefully acknowledge the work of Ana Clara Pessoa-Medeiros in preparing fuel cells for testing.

References

[1] J.C. Ely, C.R. Neal, C.F. Kulpa, M.A. Schneegurt, J.A. Seidler, J.C. Jain, Environ. Sci. Technol. 35 (2001) 3816–3822.
[2] R. Mathur, V. Balaram, M. Satyanarayanan, S.S. Sawant, S.L. Ramesh, Environ. Earth Sci. 62 (2011) 1085–1098.
[3] K. Ravindra, L. Bencs, R. Van Grieken, Sci. Total Environ. 318 (2004) 1–43.
[4] S. Chellam, Platinum Met. Environ. (2015).

[5] B. Shri Prakash, S. Senthil Kumar, S.T. Aruna, Renew. Sustain. Energy Rev. 36 (2014) 149–179.
[6] S. Aruna, M. Muthuraman, K. Patil, Solid State Ionics 111 (1998) 45–51.
[7] W.Z. Zhu, S.C. Deevi, Mater. Sci. Eng. A 362 (2003) 228–239.
[8] R.J. Gorte, J.M. Vohs, Curr. Opin. Colloid Interface Sci. 14 (2009) 236–244.
[9] S.W. Sofie, J. Am. Ceram. Soc. 90 (2007) 2024–2031.
[10] M. Boaro, J.M. Vohs, R.J. Gorte, J. Am. Ceram. Soc. 86 (2003) 395–400.
[11] H. Kim, C. da Rosa, M. Boaro, J.M. Vohs, R.J. Gorte, J. Am. Ceram. Soc. 85 (2002) 1473–1476.
[12] M.C. Tucker, G.Y. Lau, C.P. Jacobson, L.C. DeJonghe, S.J. Visco, J. Power Sources 171 (2007) 477–482.
[13] K. Araki, J.W. Halloran, J. Am. Ceram. Soc. 88 (2005) 1108–1114.
[14] T.J. Armstrong, J.G. Rich, J. Electrochem. Soc. 153 (2006) A515.
[15] W. Wang, M.D. Gross, J.M. Vohs, R.J. Gorte, J. Electrochem. Soc. 154 (2007) B439.
[16] T.L. Cable, J.A. Setlock, S.C. Farmer, A.J. Eckel, Int. J. Appl. Ceram. Technol. 8 (2011) 1–12.
[17] T.L. Cable, S.W. Sofie, J. Power Sources 174 (2007) 221–227.
[18] S.F. Corbin, X. Qiao, J. Am. Ceram. Soc. 86 (2003) 401–406.
[19] A. Buyukaksoy, V. Petrovsky, F. Dogan, J. Electrochem. Soc. 159 (2012) B232.
[20] M.C. Tucker, G.Y. Lau, C.P. Jacobson, L.C. DeJonghe, S.J. Visco, J. Power Sources 175 (2008) 447–451.
[21] A.N. Busawon, D. Sarantaridis, A. Atkinson, Electrochem. Solid-State Lett. 11 (2008) B186.
[22] K. Wiik, C.R. Schmidt, S. Faaland, S. Shamsili, M.-A. Einarsrud, T. Grande, J. Am. Ceram. Soc. 82 (2004) 721–728.
[23] S.J. Skinner, Int. J. Inorg. Mater. 3 (2001) 113–121.
[24] A. Buyukaksoy, V. Petrovsky, F. Dogan, J. Electrochem. Soc. 159 (2012) B666.
[25] T.Z. Sholklapper, H. Kurokawa, C.P. Jacobson, S.J. Visco, L.C. De Jonghe, Nano Lett. 7 (2007) 2136–2141.
[26] P. Tiwari, S. Basu, Int. J. Hydrogen Energy 38 (2013) 9494–9499.
[27] H. Kishimoto, A. Suzuki, T. Shimonosono, M.E. Brito, K. Yamaji, T. Horita, F. Munakata, H. Yokokawa, Solid State Ionics 225 (2012) 65–68.
[28] T. Klemensø, K. Thydén, M. Chen, H.J. Wang, J. Power Sources 195 (2010) 7295–7301.
[29] P. Tanasini, M. Cannarozzo, P. Costamagna, A. Faes, J. Van Herle, A. Hessler-Wyser, C. Comninellis, Fuel Cells 9 (2009) 740–752.
[30] C.H. Law, S.W. Sofie, J. Electrochem. Soc. 158 (2011) B1137.
[31] D. Driscoll, C. Hunt, J. Muretta, S.W. Sofie, ECS Trans. 53 (2013) 63–72.
[32] T.K.S. Yamaguchi, K. Kobayashi, Y. Iguchi, N. Yamada, Jpn. J. Appl. Phys. 33 (1994).
[33] S. Kurien, J. Mathew, S. Sebastian, S.N. Potty, K.C. George, Mater. Chem. Phys. 98 (2006) 470–476.
[34] R.W. Clark, P. Wynblatt, J.K. Tien, Acta Metall. 30 (1982) 139–146.
[35] H. Provendier, C. Petit, C. Estournès, S. Libs, A. Kiennemann, Appl. Catal. A: Gen. 180 (1999) 163–173.
[36] H.C. Ling, A.M. Jackson, IEEE Trans. Compon. Hybrids, Manuf. Technol. 12 (1989) 130–137.
[37] R. Davis, F. Abdeljawad, J. Lillibridge, M. Haataja, Acta Mater. 78 (2014) 271–281.
[38] D. Driscoll, A.J. Weisenstein, S.W. Sofie, Mater. Lett. 65 (2011) 3433–3435.
[39] W. Brockner, C. Ehrhardt, M. Gjikaj, Thermochim. Acta 456 (2007) 64–68.
[40] A. Lussier, S. Sofie, J. Dvorak, Y.U. Idzerda, Int. J. Hydrogen Energy 33 (2008) 3945–3951.
[41] A. Mai, V.A.C. Haanappel, S. Uhlenbruck, F. Tietz, D. Stöver, Solid State Ionics 176 (2005) 1341–1350.
[42] S. Simner, J. Bonnett, N. Canfield, K. Meinhardt, J. Shelton, V. Sprenkle, J. Stevenson, J. Power Sources 113 (2003) 1–10.
[43] B.L. Augusto, F.B. Noronha, F.C. Fonseca, F.N. Tabuti, R.C. Colman, L.V. Mattos, Int. J. Hydrogen Energy 39 (2014) 11196–11209.
[44] M.B. Pomfret, J.C. Owrutsky, R.A. Walker, Annu. Rev. Anal. Chem. 3 (2010) 151–174.
[45] M.B. Pomfret, J.C. Owrutsky, R.A. Walker, J. Phys. Chem. B Lett. 110 (2006) 17305–17308.
[46] Y.K. Sharma, M. Kharkwal, S. Uma, R. Nagarajan, Polyhedron 28 (2009) 579–585.
[47] F. Azough, R. Freer, J. Petzelt, J. Mater. Sci. 28 (1993) 2273–2276.
[48] A. Kaiser, A.J. Feighery, D.P. Fagg, J.T.S. Irvine, Ionics (Kiel) 4 (1998) 215–219.
[49] E. López-López, M.L. Sanjuán, R. Moreno, C. Baudín, J. Eur. Ceram. Soc. 30 (2010) 981–991.
[50] P. Bordet, A. McHale, A. Santoro, R.S. Roth, J. Solid State Chem. 64 (1986) 30–46.
[51] E. López-López, M.L. Sanjuán, R. Moreno, C. Baudín, J. Eur. Ceram. Soc. 30 (2010) 981–991.
[52] T.A. Schaedler, W. Francillon, A.S. Gandhi, C.P. Grey, S. Sampath, C.G. Levi, Acta Mater. 53 (2005) 2957–2968.
[53] J.M. Santamaria, E.E. Miro, E.E. Wolf, Ind. Eng. Chem. Res. 30 (1991) 1157–1165.
[54] P. Salvador, J. Appl. Phys. 53 (1982) 7003.
[55] L.S.M. Traqueia, T. Pagnier, F.M.B. Marques, J. Eur. Ceram. Soc. 17 (1997) 1019–1026.
[56] Z. Liu, B. Liu, D. Ding, M. Liu, F. Chen, C. Xia, J. Power Sources 237 (2013) 243–259.
[57] C.L. Wang, H.Y. Lee, F. Azough, R. Freer, J. Mater. Sci. 32 (1997) 1693–1701.
[58] E. Çitak, T. Boyraz, Acta Phys. Pol. A 125 (2014) 465–468.